Article

High-Resolution Remote Sensing Images Can Better Estimate Changes in Carbon Assimilation of an Urban Forest

Qing Huang [1], Xuehe Lu [2,*], Fanxingyu Chen [2], Qian Zhang [3,4] and Haidong Zhang [5]

[1] School of Environmental Science, Nanjing Xiaozhuang University, Nanjing 211171, China
[2] School of Geography Science and Geomatics Engineering, Suzhou University of Science and Technology, Suzhou 215009, China
[3] School of Geomatics Science and Technology, Nanjing Tech University, Nanjing 211816, China
[4] State Key Laboratory of Soil Erosion and Dryland Farming on the Loess Plateau, Institute of Soil and Water Conservation, Northwest A&F University, Yangling 712100, China
[5] Institute of Agricultural Sciences in Taihu Area of Jiangsu, Suzhou 215155, China
* Correspondence: luxh@usts.edu.cn

Abstract: Urban forests have the potential to sink atmospheric CO_2. With the improvement of coverage of vegetation in urban environments, more attention has been paid to the carbon sequestration potential of the urban forest. However, the high fragmentation of urban forests makes it difficult to evaluate their carbon budget on a regional scale. In this study, the GPP-NIRv relationship model was employed to estimate GPP in Suzhou by MODIS, Landsat-8 and Sentinel-2 remote sensing data, and to further explore what kind of remote images can figure out the spatial-temporal pattern of GPP in urban forests. We found that the total GPP of the terrestrial ecosystem in Suzhou reached 8.43, 8.48, and 9.30 Tg C yr-1 for MODIS, Landsat-8, and Sentinel-2, respectively. Monthly changes of GPP were able to be derived by MODIS and Sentinel-2, with two peaks in April and July. According to Sentinel-2, urban forests accounted for the majority of total GPP, with an average of about 44.63%, which was larger than the results from GPP products with coarser resolutions. Additionally, it is clear from the high-resolution images that the decline of GPP in May was due to human activities such as the rotation of wheat and rice crops and the pruning of urban forests. Our results improve the understanding of the contribution of the urban forest to the carbon budget and highlight the importance of high-resolution remote sensing images for estimating urban carbon assimilation.

Keywords: gross primary productivity; near-infrared reflectance of vegetation; urban forest; carbon budget

1. Introduction

Gross Primary Productivity (GPP) quantifies the total amount of carbon assimilated by plants through photosynthesis per unit time. As the critical variable of carbon cycling of terrestrial ecosystems, GPP is the initial amount of energy and material entering the terrestrial ecosystem and plays an essential role in regulating the global carbon cycle [1–3]. GPP can be observed at the leaf level or ecosystem level [4–6], and also can be simulated by process-based terrestrial ecosystem models [7–9] or estimated through remote sensing [10–13]. Benefiting from the eddy-covariance techniques and the multisource data of remote sensing, satellite-based GPP models were developed to estimate regional and global GPP by establishing the empirical relationship between the vegetation index (VI) and surface observation data [14–18]. Previous studies have shown that the correlation coefficient between Enhanced Vegetation Index (EVI) and surface observation data in global GPP estimation can reach 0.52–0.92 [19], and the correlation coefficient between Solar-induced Chlorophyll Fluorescence (SIF) and GPP for crops and grass can achieve 0.87 [20]. However, there are several limitations in these methods; for example the adaptability of the empirical method is affected by different ecosystem structures and climate conditions [21].

Additionally, the coarse spatiotemporal resolution of satellite SIF is generally a limiting factor in the regional estimation of GPP [22,23].

In recent years, Near-infrared Reflectance of Vegetation (NIRv), which integrates the advantages of NDVI and near-infrared reflectance, has provided a new avenue for GPP estimation [24–27]. NDVI can intuitively reflect vegetation coverage, which is tightly correlated to vegetation productivity, while near-infrared reflectance can embody the information on vegetative canopy structure and leaf area [24,28]. Therefore, NIRv takes into consideration both the pigment and structure of vegetation in remote sensing images to avoid the saturation effects of NDVI [29–31]. Meanwhile, a strong and stable correlation was found between NIRv and GPP in the same ecosystem [21,23,32]. In the study of regional and global carbon budgets of terrestrial ecosystems, NIRv has been suggested as the effective substitution for satellite SIF, based on theoretical derivations and radiative transfer simulations, and has gained a great deal of attention in recent years [24,33].

Urban forest is considered as a large green infrastructure in the urban area, which consists of trees, shrubs and grasses in streets, parks, gardens, alongside rivers and so on [34–36]. Additionally, urban forest in this study is also defined as the above description. Urban forest usually plays an indispensable role for people living in urban environments, such as reducing air pollution and heat islands effect [37], and increasing biodiversity [38]. As global CO_2 concentrations continue to increase, there is also increasing interest in the carbon storage and sequestration of the urban forest [39–41]. Vegetation in urban areas is offered for environments with higher temperatures and CO_2 concentrations, highly intensive use of water and pesticides [42,43], and its photosynthetic activity would play an important role in the carbon cycle of terrestrial ecosystems.

However, in some studies, the vegetation productivity in urban areas was set as zero [44]; the role of urban vegetation might be underestimated in the global carbon budget. With the improvement of urban green coverage (e.g., the green coverage in the urban built areas in Jiangsu province increased from 19.5% in 1990 to 42.1% in 2020), more attention should be paid to the effect of the urban forest in the global and regional carbon assimilation [45–47]. Although the ability of carbon assimilation can be estimated through GPP, the contribution of the urban forest to regional carbon assimilation is still unclear. A number of difficulties in the current estimations of urban GPP need to be overcome; for example the lack of surface observation data in urban areas makes it difficult to conduct empirical estimation on the urban scale by using traditional VI. At the same time, the lack of driving and parameterized data with high spatiotemporal resolution significantly reduced the performance of process-based ecological models in the simulation of GPP in urban areas.

As NIRv has successfully estimated GPP in other ecosystems, it may be able to provide a new approach to estimating carbon assimilation in urban forests. To the best of our knowledge, the contribution of urban forests to regional carbon assimilation has not yet been studied according to this method. Meanwhile, it is not yet clear which resolution of satellite data is appropriate for determining urban forest carbon assimilation capacity. Therefore, in this study, the GPP-NIRv relationship model is employed to estimate the GPP of terrestrial ecosystems in Suzhou by MODIS, Landsat-8, and Sentinel-2 remote sensing data, and to further explore what kind of remote images can figure out the spatiotemporal pattern of GPP of urban forests. Then, we evaluate the contribution of urban forest to the regional carbon budgets and the impact of human activities on regional GPP. The expected results will improve our understanding of the ability of urban forests to affect carbon assimilation and will provide an appropriate reference for selecting the right resolution of remote sensing images for carbon budget research in urban areas.

2. Materials and Methods

2.1. Study Area

Suzhou is one of the most economically developed cities in eastern China, and is located in the southeast of Jiangsu and the middle of the Yangtze River Delta, with the

region ranging from eastern longitude 119°55′ to 121°20′ and northern latitude from 30°47′ to 32°02′. Suzhou connects to Shanghai to the east, Jiaxing and Huzhou of Zhejiang province to the north, Wuxi to the west, and the Yangtze River to the north, with a total area of 8657.32 km². As one of the largest industrial cities in China, Suzhou has an urban population of 12.84 million, and the gross output value of all the above designated-size industrial enterprises in Suzhou exceeded CNY 4 trillion in 2021 (http://tjj.suzhou.gov.cn/sztjj/tjnj/2021/zk/indexce.htm (accessed on 1 May 2022)).

Suzhou lies in the subtropical monsoon climate zone, where abundant precipitation and warm temperatures are suitable for vegetation growth. The annual precipitation and mean temperature in the year 2021 were 1318.6 mm and 18.3 °C, respectively. Suzhou is low and even, with a general elevation range from 3.5 to 5 m above sea level. The southeast of Suzhou is lower, with the lowest elevation below 2 m, and the southwest is a hilly area where vegetation grows well. The terrain of this area is shown in Figure 1. Suzhou is a famous water country region with a dense river network and numerous lakes, and rivers, lakes, tidal flats and wetlands account for 34.6% of the total area. Cropland is the dominant land use type in Suzhou, with an area of about 2871.6 km², accounting for 33.17% of the total area.
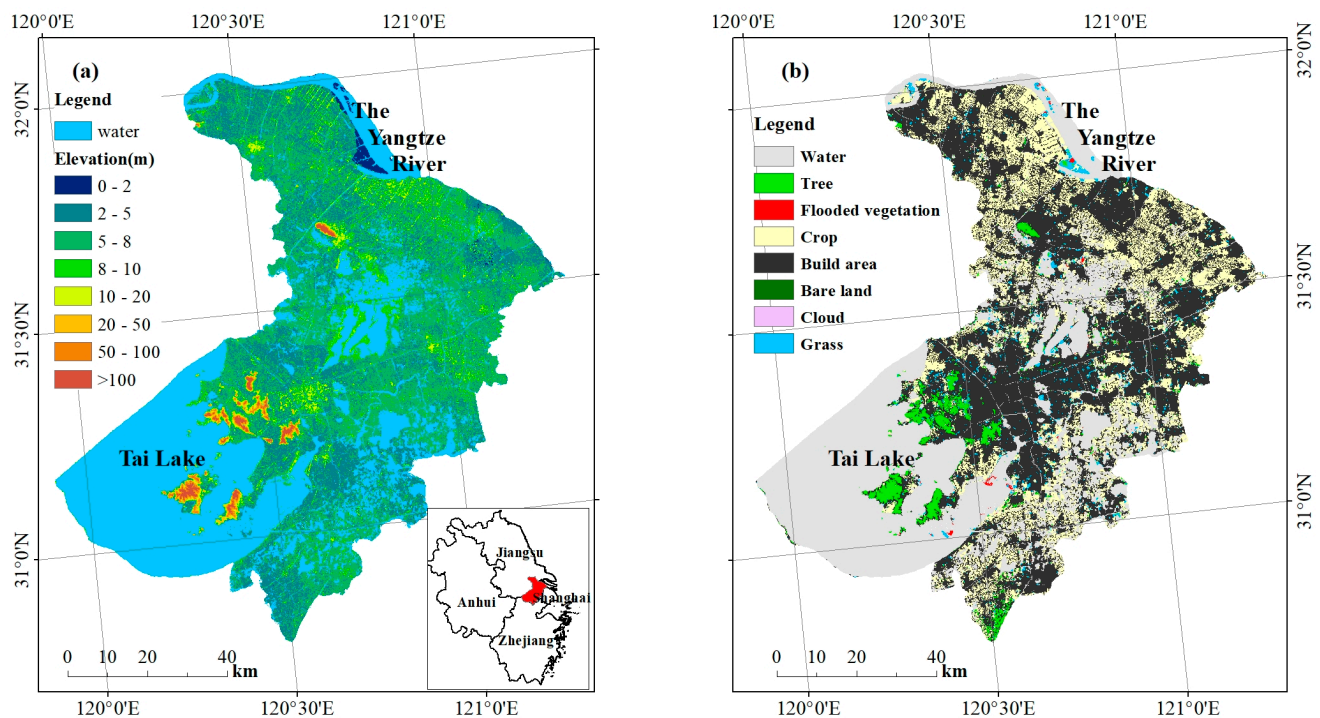

Figure 1. The geographic location (**a**) and land cover (**b**) derived from Sentinel-2 by ESRI of Suzhou in Jiangsu province in China.

2.2. Data Sources and Processing

Remote sensing data, climate data and land cover data were used in this research to estimate GPP in Suzhou and analyze the importance of urban forests for the regional carbon budget. Three kinds of resolution remote sensing images are used to estimate GPP. Of these, 30 m-Landsat 8 and 10 m-Sentinel 2 surface reflectance datasets were downloaded from the United States Geological Survey (https://earthexplorer.usgs.gov/ (accessed on 10 April 2022)) and the Copernicus Open Access Hub (https://scihub.copernicus.eu/dhus/#/home (accessed on 15 April 2022)) in 2021 to calculate NIRv. In order to avoid the impact of cloud on data quality, the maximum value composite (MVC) method was set to generate the monthly NIRv.

MODIS 500 m surface reflectance data (MOD09A1) and NDVI data (MOD13A1) downloaded from NASA's Distributed Active Archive Center (DAAC) have eliminated the

impact of cloud. In order to maintain the consistency of the production of NIRv, the MVC method was also used to generate the MODIS monthly NIRv.

Climate data, including monthly temperature and precipitation, were used to investigate GPP changes in response to the local climate; climate data were obtained from the National Meteorological Science Data Center (https://data.cma.cn/ (accessed on 2 May 2022)).

MODIS, Landsat and Sentinel-2 land cover datasets were downloaded to summarize the GPP of different land cover types according to the corresponding estimation of GPP with the same spatial resolution. A MODIS land cover data (MCD12Q1) product was downloaded from NASA DAAC. The MCD12Q1 product supplies maps of land cover at annual steps, and the land cover in Suzhou was classified according to the International Geosphere Biosphere Programme (IGBP) land cover classification scheme as urban and built-up lands, croplands, grasslands, water bodies, evergreen broadleaf forests (EBF), deciduous broadleaf forest (DBF), mixed forest (MF) and so on.

Global land cover data producing 30 m resolution were downloaded from http://data.ess.tsinghua.edu.cn/ (accessed on 17 April 2022). This product used the amount of training samples across the world to optimize many kinds of classifiers, eg. maximum likelihood, decision tree, random forest, etc. A unique land-cover classification system was used in this product. In Suzhou, the typical land cover types were crop, forest, grass, shrub, water, and impervious. Additionally, impervious was considered as urban built-up areas in this study.

ESRI generated a global map of land use and land cover (https://livingatlas.arcgis.com/landcover/ (accessed on 17 April 2022)) derived from Sentinel-2 imagery at 10 m resolution by using a deep learning AI land classification model trained by billions of human-labeled image pixels [48]. This product has 9 classes, of which water, tree, crop, shrub land, built area and grass are the dominant ones in Suzhou.

In order to better calculate the changes in carbon assimilation of urban forest, the urban area of Suzhou was divided into built area (black areas in Figure 1b) and non-built area (remaining areas besides built area).

2.3. Estimation of GPP

NIRv has been found to accurately capture both the seasonal and annual variation in GPP at flux sites [25,26]. GPP correlates linearly with NIRv among different vegetation types (Table S1), and global GPP was estimated with high accuracy on a monthly basis by upscaling the relationships between NIRv and GPP [23]. In this study, we also use these correlations to determine the Suzhou monthly GPP based on NIRv, and the calculation of NIRv and GPP are shown in Equations (1) and (2):

$$NIRv = \frac{NIR - R}{NIR + R} \times NIR \qquad (1)$$

$$GPP = a \times NIRv + b \qquad (2)$$

R and *NIR* are the red and the near-infrared bands, *a* and *b* are derived from linear regression, and the values can be found in Table S1. We used the MVC method to generate the monthly NIRv. Landsat-8 has a limited frequency of revisits, so some images were lost during the rainy season, i.e., in July and August. MODIS and Sentinel-2 had sufficient data to produce a full image each month.

For different kinds of forests, such as deciduous broadleaf forests (DBF), evergreen broadleaf forests (EBF), evergreen needle forests (ENF), and mixed forests (MF), Wang et al. [23] used different coefficients for calculating GPP. However, the land cover data of Sentinel-2 used in this study do not distinguish forest type. As a result, based on the studies of [49], changes in tree NDVI between summer and winter were examined to determine the forest types, including deciduous broadleaf forest, mixed forest and evergreen broadleaf forest, according to the criteria listed in Criteria 2 of Table 1. Additionally, we did not include evergreen needle forest in calculating GPP, for the reason that its distribution in

Suzhou is limited and hard to separate from evergreen broadleaf forests by only the change in NDVI. Considering that the grassland and different kinds of forests in urban area are always integrated but still able to be identified according to dominated coverage of plants, vegetation types of urban forest in built area were also identified as grass (GRA), DBF, MF and EBF.

Table 1. NDVI for identifying vegetation type in land cover of tree and built area.

NO.	Criteria 1	Criteria 2	TR	BA	Veg
1	$NDVI_8 < 0.2$			C1 and 2	BRE
2	$0.2 \leq NDVI_8 < 0.5$			C1 and 2	GRA
3	$0.5 \leq NDVI_8 \leq 1$	$(NDVI_8 - NDVI_{12})/NDVI_8 > 0.35$	C2	C1 and 2	DBF
4	$0.5 \leq NDVI_8 \leq 1$	$0.2 < (NDVI_8 - DVI_{12})/NDVI_8 < 0.35$	C2	C1 and 2	MF
5	$0.5 \leq NDVI_8 \leq 1$	$(NDVI_8 - NDVI_{12})/NDVI_8 < 0.2$	C2	C1 and 2	EBF

Note: The subscript is month, $NDVI_8$ and $NDVI_{12}$ are monthly NDVI in August and December. C1 and C2 are criteria 1 and criteria 2, respectively. Veg is the vegetation type. TR and BA are the land cover of tree and built area. BRE and GRA are bare land and grass land, respectively.

In the built area, the contribution of urban forests to total regional carbon assimilation cannot be ignored as they are widely distributed in Suzhou. However, they are usually buried in lower-resolution imagery. Considering the fragmentation of urban forests, three different resolutions of remote images, i.e., MODIS, Landsat and Sentinel-2, were used to evaluate the ability to detect urban forests. For calculating GPP in urban forest, NDVI changes in the built area were used to determine vegetation types as shown in Criterions 1 and 2 of Table 1.

2.4. Data Analysis

Based on our estimation, the GPPs of different land cover types were summarized according to land cover data. Then, we identified the contribution of urban forests to the regional total GPP. Vegetation in urban areas is inevitably affected by human activities. Therefore, the monthly changes of GPP were examined to find out the abnormal fluctuation of monthly GPP and identify what kind of human activities disturbed the change in GPP.

3. Results

3.1. Variance of NIRv in Different Remote Sensing Data with Distinct Spatial Resolutions

The NIRv can be calculated based on MODIS, Landsat-8 and Sentinel-2 by using Equation (1). Figure 2 shows the spatial distribution of Sentinel-2 NIRv monthly.

The area along the Yangtze River in the northern part of Suzhou was a high-value area of NIRV. Additionally, the changes in NIRv in this area were significantly greater than in other parts of the city. During the growing season, in April and from July to September, NIRv reached more than 0.45. The high NIRv value in this area was a result of the high photosynthetic ability of crops planted in this region, for example, wheat and rice. Furthermore, around Tai Lake, the large water body in the southwest of the city, there was another area with a high NIRv. Forests and crops were spread throughout this area (Figure 1b), and the peak NIRv was around 0.4 from June to August.

The NIRv in Suzhou's built area ranged from 0 to 0.1, generally, without an evidently monthly dynamic. Nevertheless, there were many points scattered in the built area with high NIRvs (ranging from 0.2 to 0.35) and also seasonal changes. The urban forest in built areas contributed to the scattered high-value points. This kind of vegetation is usually found in small urban green spaces, and was represented as discrete points by remote sensing data with high resolution.
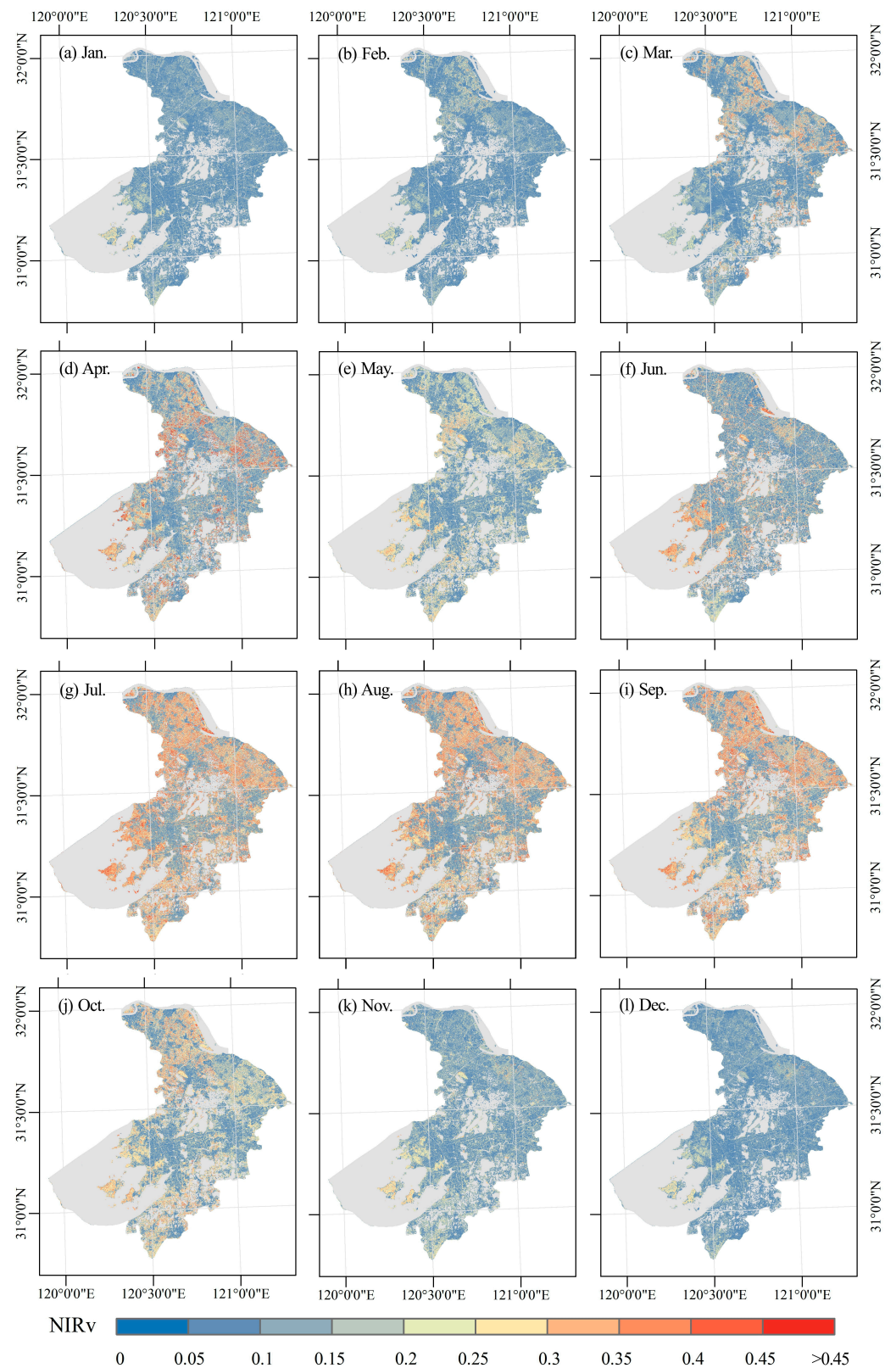
Figure 2. Spatial distribution of monthly Sentinel-2 NIRv in 2021, Suzhou.

For comparing the differences of NIRv derived from MODIS, Landsat-8 and Sentinel-2, the monthly averages and standard deviations of NIRv were listed in Figure 3. Sentinel-2 NIRv showed two peaks in April and July, with values of 0.13 and 0.18, respectively. The values of MODIS NIRv were generally lower than Sentinel-2 and had similar trends to

Sentinel-2. Due to the impact of the cloud, the continuous change of Landsat-8 NIRv was hard to obtain. Additionally, current valid data of Landsat-8 were similar to MODIS NRIv and also showed a peak in September.
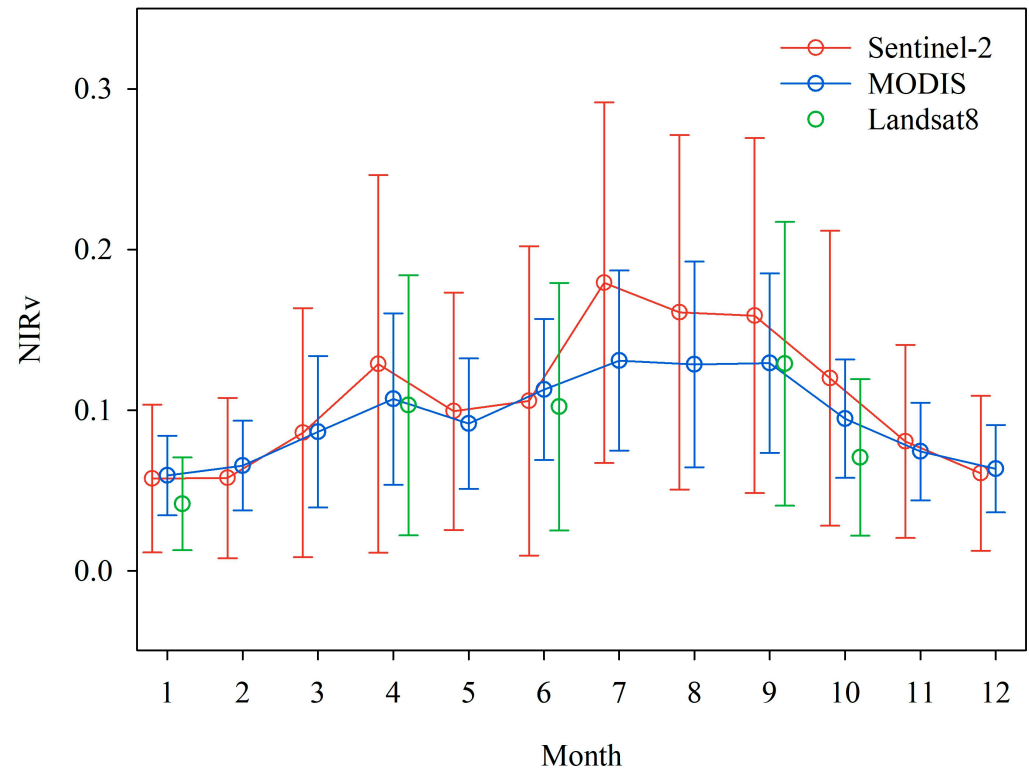

Figure 3. Monthly averages (red, blue and green cycle) and standard deviations (red, blue and green bar) of NIRv in Suzhou derived from MODIS, Landsat-8 and Sentinel-2.

3.2. Comparing the GPPs Estimated by Different Resolutions of Remote Sensing Data

The GPPs estimated by NIRv derived from MODIS, Landsat-8 and Sentinel-2 were shown in Table 2. The total GPP in Suzhou in 2021 estimated by MODIS, Landsat-8 and Sentinel-2 was 8.43, 8.48, and 9.30 Tg C yr^{-1} (Tg = 10^{12} g), respectively. Our estimations of GPP were higher than the results of MOD17A2 (4.37 Tg C yr^{-1}), which ignores the contribution of the urban forest in built areas (black areas in Figure 4a). In contrast, our results included this ignoring component and fell within the range of previous studies which considered the contribution of urban forest (Table 2).

Table 2. Comparison of urban contribution to GPP in different GPP products.

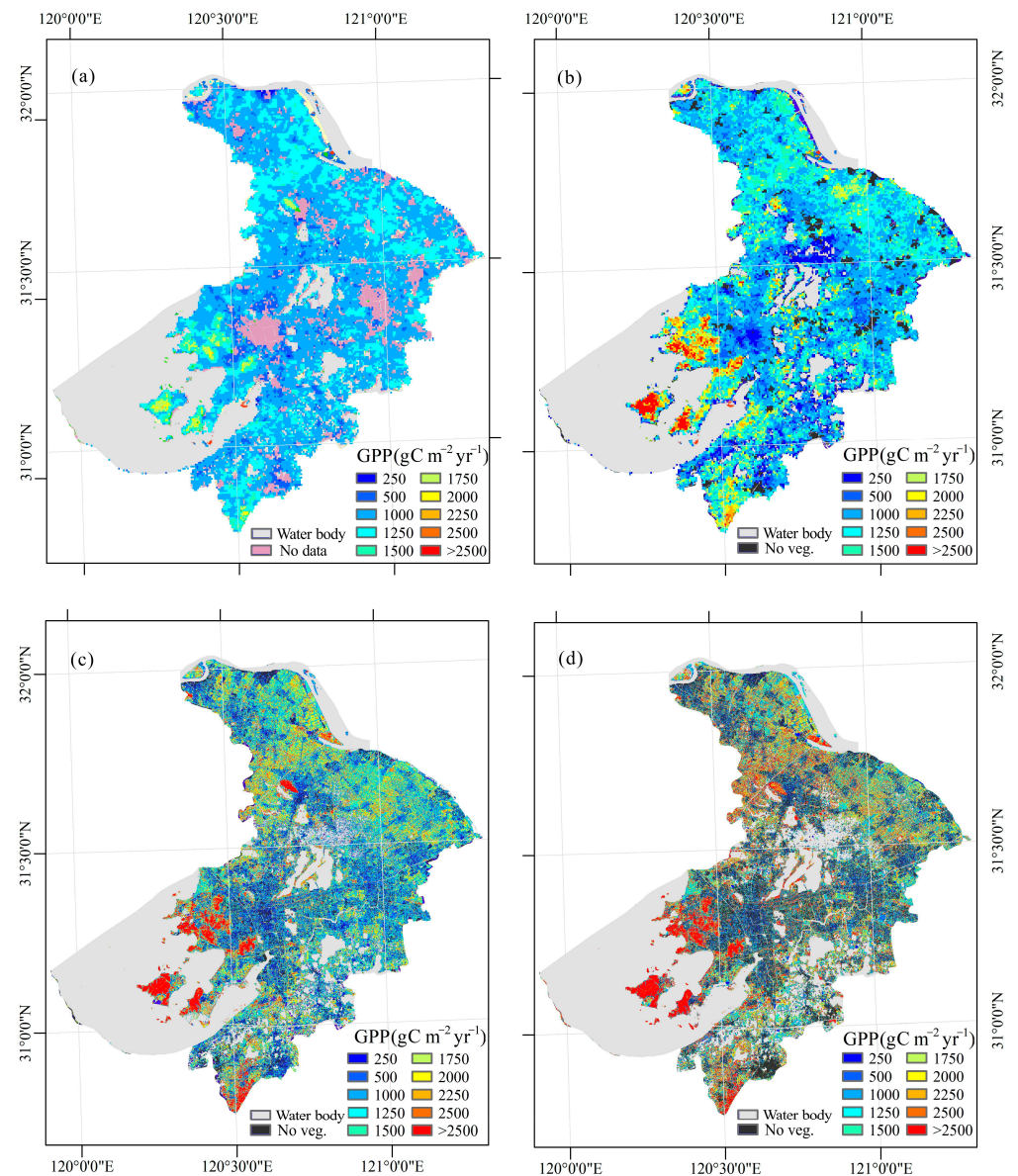| Product	Resolution	Time	Model	Total GPP (Tg C)	Remark
This Study	10 m	2021	NIRv-GPP	9.30	Sentinel-2
	30 m	2021		8.48	Landsat8
	500 m	2021		8.43	MODIS
MOD17A2	500 m	2021	LUE	4.37	
Zhang [50]	0.050°	2016	VPM	9.37	
Ju [51]	0.073°	2019	BEPS	6.72	

Figure 4. The spatial distribution of GPP from MOD17A2 product (**a**) and estimated by MODIS (**b**), Landsat-8 (**c**), Sentinel-2 (**d**). Areas in panel (**a**) with no data are due to the MODIS product not calculating GPP if the land cover type is built area. Additionally, the no vegetation (veg.) areas in panels (**b–d**) are the regions where the NDVI is less than 0.2 and, as a result, is recognized as bare land with no GPP.

The spatial patterns of GPP in Suzhou estimated by MODIS, Landsat-8 and Sentinel-2 in 2021 were shown in Figure 4b–d. All three kinds of GPP showed the same high GPP region located around Tai Lake (grey area in the southwest of Figure 4). In many areas of this region, the GPP ranged from 2500 to 3000 g C m^{-2} yr^{-1}. The estimated GPPs had some differences in the northeast, along the Yangtze River (grey area in the northeast of Figure 4). In this region, the GPP of MODIS was lower than the GPP of Landsat-8 and Sentinel-2. According to our MODIS GPP results, most built areas were capable of photosynthesis from the vegetation within them. Additionally, GPP in built area of Suzhou ranged from 250 to 500 g C m^{-2} yr^{-1}. Ignoring the contribution of GPP from the built area (black area in Figure 4a) induced the lower GPP in MOD17A2. Furthermore, high-resolution results from Landsat-8 and Sentinel-2 also indicated the contribution of urban forests, which were scattered over the built area due to their spatial distribution being highly discrete in Suzhou (Figure 4c,d).

3.3. Monthly Change of GPP in the Year 2021

The Landsat-8 GPP failed to overcome the effects of clouds every month since its long revisit. Additionally, with the help of the MVC method, monthly NIRvs derived by MODIS and Sentinel-2 were generated. As a result, Figure 5 shows only the MODIS and Sentinel-2 GPPs, as well as the changes in monthly temperature and precipitation for the year 2021.
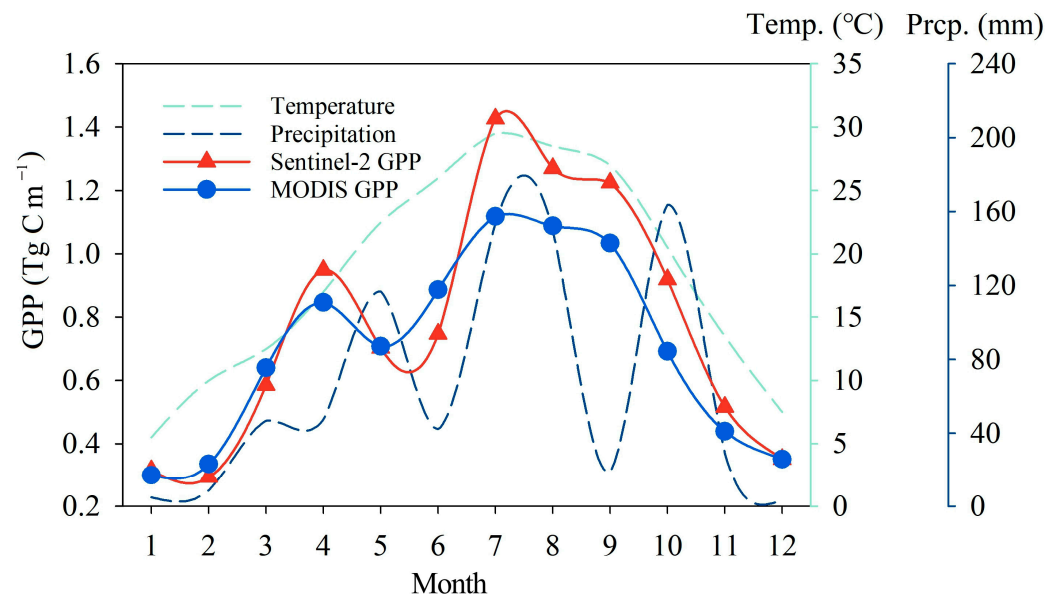

Figure 5. The monthly change of Suzhou's GPP in the year 2021.

The monthly GPP of MODIS and Sentinel-2 showed two peaks in 2021. One peak was in April, with GPPs 0.85 and 0.95 Tg C m^{-1} for MODIS and Sentinel-2, respectively. The other peak was in July, when the GPPs of MODIS and Sentinel-2 reached their summit for the whole year: 1.43 and 1.12 Tg C m^{-1}, respectively. Between the two peaks was an evident decrement in GPP in May. GPP decreased by 16.4% and 25.9% according to the estimations of MODIS and Sentinel-2, respectively.

In the growing season, the MODIS GPP was generally lower than Sentinel-2 GPP. For example, from July to September, the average of Sentinel-2 GPP was 1.31 Tg C m^{-1}, which was 21.3% higher than MODIS GPP in the same period. Additionally, a similar difference was also found in the growing peak in April. Moreover, in winter and early spring MODIS GPP and Sentinel-2 GPP were similar.

As Figure 6 showed, a significant ($p < 0.001$) linear relationship was found between the air temperature and GPP. R^2 for the temperature–GPP relationships were 0.81 and 0.89 for Sentinel-2 and MODIS GPP, respectively (Figure 6a,b), which was higher than the precipitation–GPP relationship (Figure 6c,d). Therefore, the change in GPP was mainly determined by the air temperature in the year 2021. Additionally, the positive coefficient of slopes for the linear relationships indicated that temperature and precipitation had positive effects on GPP. However, the GPP declined when temperature and precipitation increased in May. This decrement in GPP implies that, besides climatic factors, some other factors determined the change in GPP in May. In urban areas, the impact of anthropogenic activities on vegetation cannot be ignored.
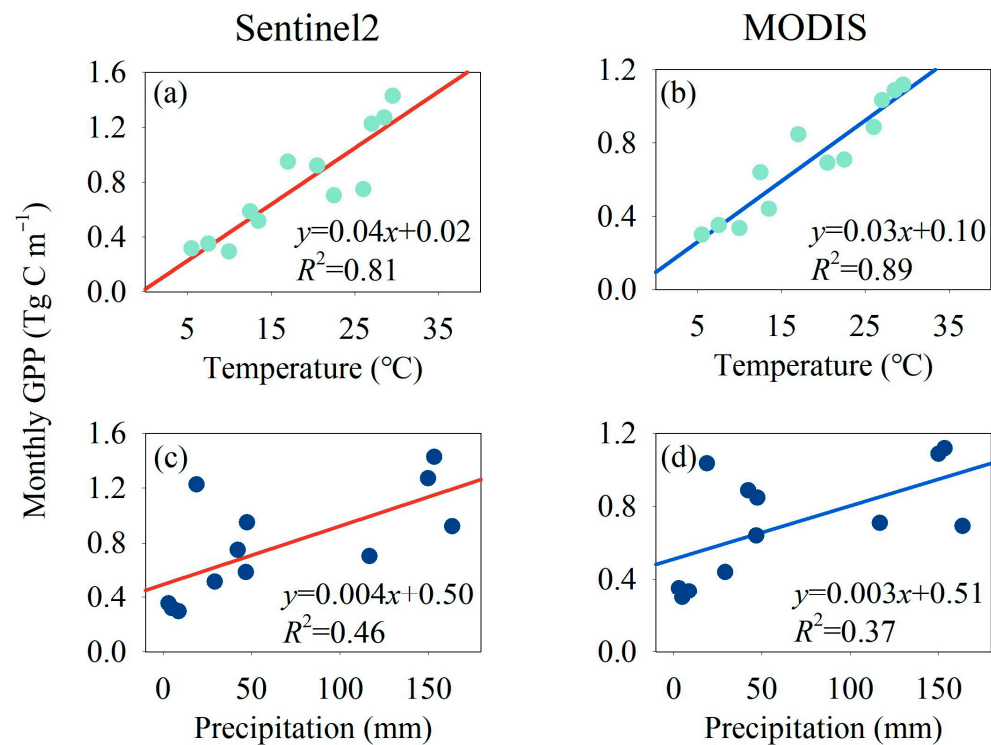
Figure 6. The relationship between the estimated GPP and climate factors. (**a**) and (**b**) are the correlations between temperature and monthly GPP for Sentinel2 and MODIS, respectively. (**c**) and (**d**) are the correlations between precipitation and monthly GPP for Sentinel2 and MODIS, respectively.

3.4. Changes in GPP of Different Land Cover Types

To better understand the importance of urban forests to the regional GPP, the Sentinel-2 and MODIS GPP changes in different land cover types were shown in Figure 7. According to the result of Sentinel-2, the average monthly GPP of vegetation in the built area (e.g., urban forest) and non-built area (e.g., crop, tree, grassland) was 0.35 Tg C and 0.43 Tg C (0.32 for crops, 0.08 for trees, and 0.03 Tg C for grassland), respectively. Additionally, for MODIS, GPP of the built area and non-built area was 0.28 Tg C and 0.42 Tg C (0.18, 0.01, and 0.23 Tg C for crop, tree, and grassland, respectively). The MODIS GPP of grassland was 0.20 Tg C higher than Sentinel-2 GPP, and the MODIS GPP of cropland was 0.14 Tg C lower than Sentinel-2 GPP. This may be caused by the use of different land cover datasets in statistics. MODIS land cover products might be misplaced between farmland and grassland due to the lower spatial resolution. In fact, as an industrialized city, Suzhou does not have a lot of grasslands.

The GPP of each land cover type varied throughout the year (Figure 7a,c). Similar to the change in total GPP, each land cover type had two peaks in spring and summer. Additionally, they also showed decrements in GPP in May. These decrements in GPP for crops and urban forests were obviously about 32.33% and 23.57%, respectively, according to Sentinel-2 GPP.

Sentinel-2 results indicated that crops and urban forests accounted for a majority of the total GPP in Suzhou in 2021, with an average of about 38.15% and 44.43%, respectively. Trees and grasses in non-built area made relatively small contributions to total GPP, accounting for approximately 11.87% and 4.17%, respectively. According to MODIS GPP, urban forests still accounted for the majority (39.66%) of total GPP, followed by grassland and crops at 33.66% and 25.60%, respectively.
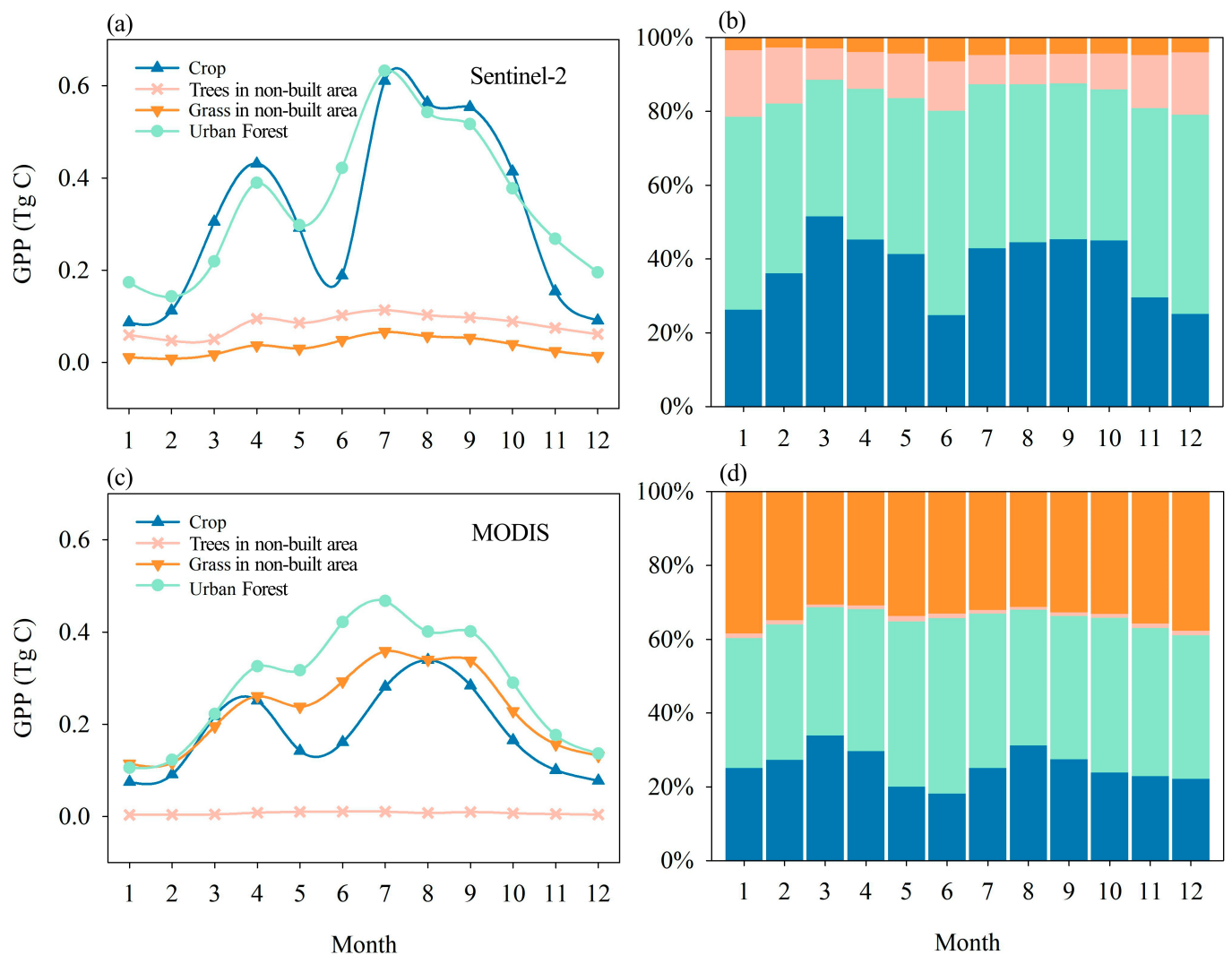
Figure 7. The Sentinel-2 and MODIS GPP changes in different land cover types in 2021 (**a**,**c**) and their contribution to total GPP (**b**,**d**).

The contribution of different land cover types also varied throughout the year (Figure 7b,d). Taking the most contributed urban forests as an example, their Sentinel-2 GPP exceeded 50% of the total GPP for five months of the year, with the highest percentage at 55.39% in June. Additionally, the contribution made by crops was also large, even more than the contribution of urban forests in growing peak seasons, such as April and August.

3.5. Changes in GPP by Anthropogenic Factors

The spatial distribution of this decrement in GPP in May is shown in Figure 8. The evident decrement of GPP for the crop was mainly in the rice and wheat rotation area along the Yangtze River. In May, as wheat matures, its photosynthetic capacity also decreases significantly. Additionally, in June, after the wheat harvest, rice has just been planted. In consequence, the photosynthetic capacity had not yet recovered.
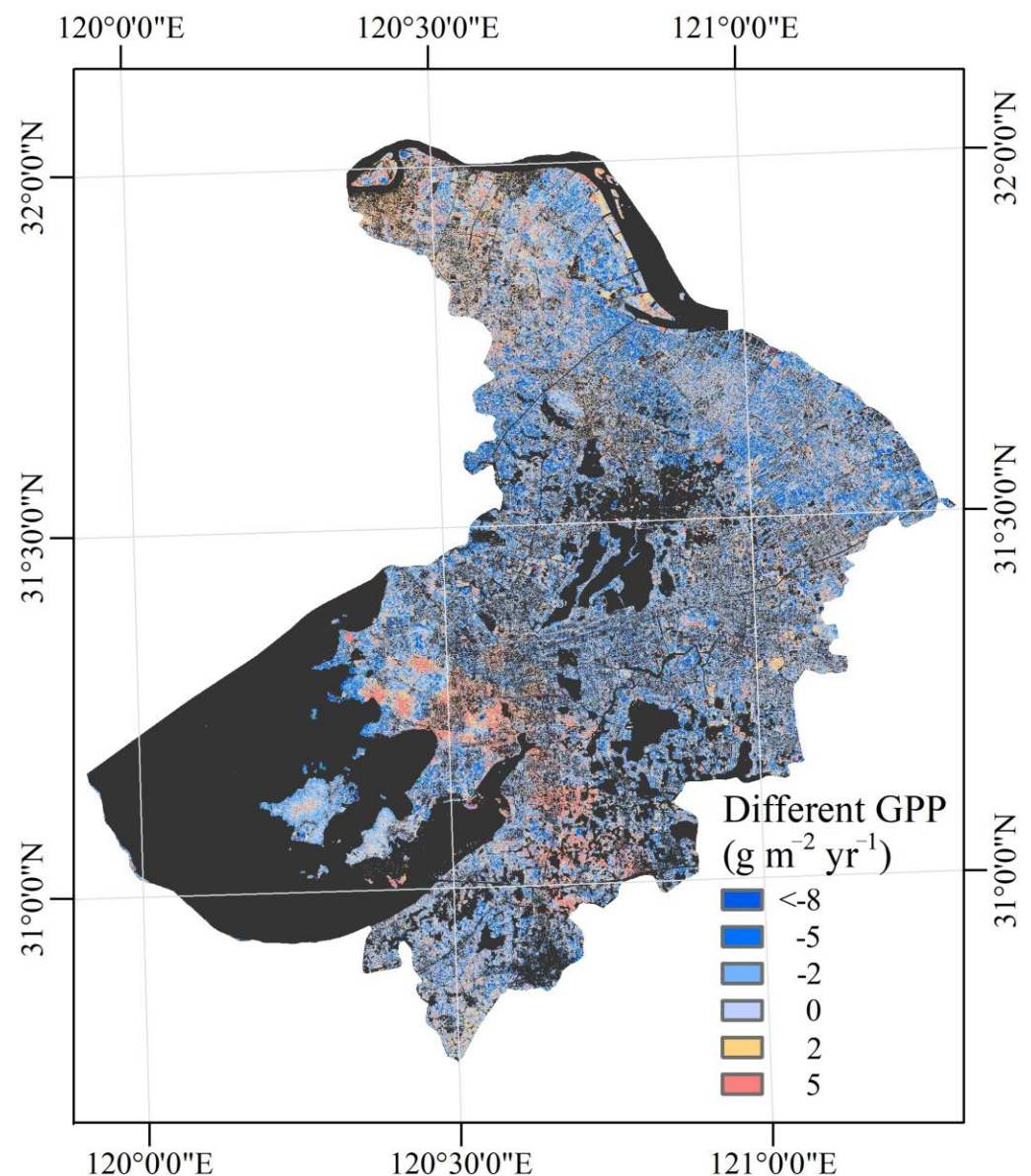
Figure 8. The difference in GPP between April and May in Suzhou.

Furthermore, urban forests' GPP also decreased significantly in May, but recovered quickly in June (Figure 7a,c). For making urban vegetation more attractive, urban forests in Suzhou undergo a pruning process in May. This process removes a considerable amount of leaves from the canopy. Usually, these leaves are current-year leaves and are located at the top of the canopy. Additionally, the photosynthetic capacity of these kinds of leaves is greater than that of old leaves and lower canopy leaves [52,53]. The pruning process is usually conducted on the grassland and shrub land, which were the main parts of urban green spaces in Suzhou, approximately 55.67% (Figure 9) according to our criteria in Table 1. Haberl [54] proposed that the averaged biomass loss during gardening (such as pruning) or park and infrastructure maintenance amounted to 50% of the aboveground Net Primary Productivity (the remainder of GPP deducts autotrophic respiration). Therefore, the pruning process removes the most photosynthetic part of the canopy, which results in the decline of GPP of urban forests.
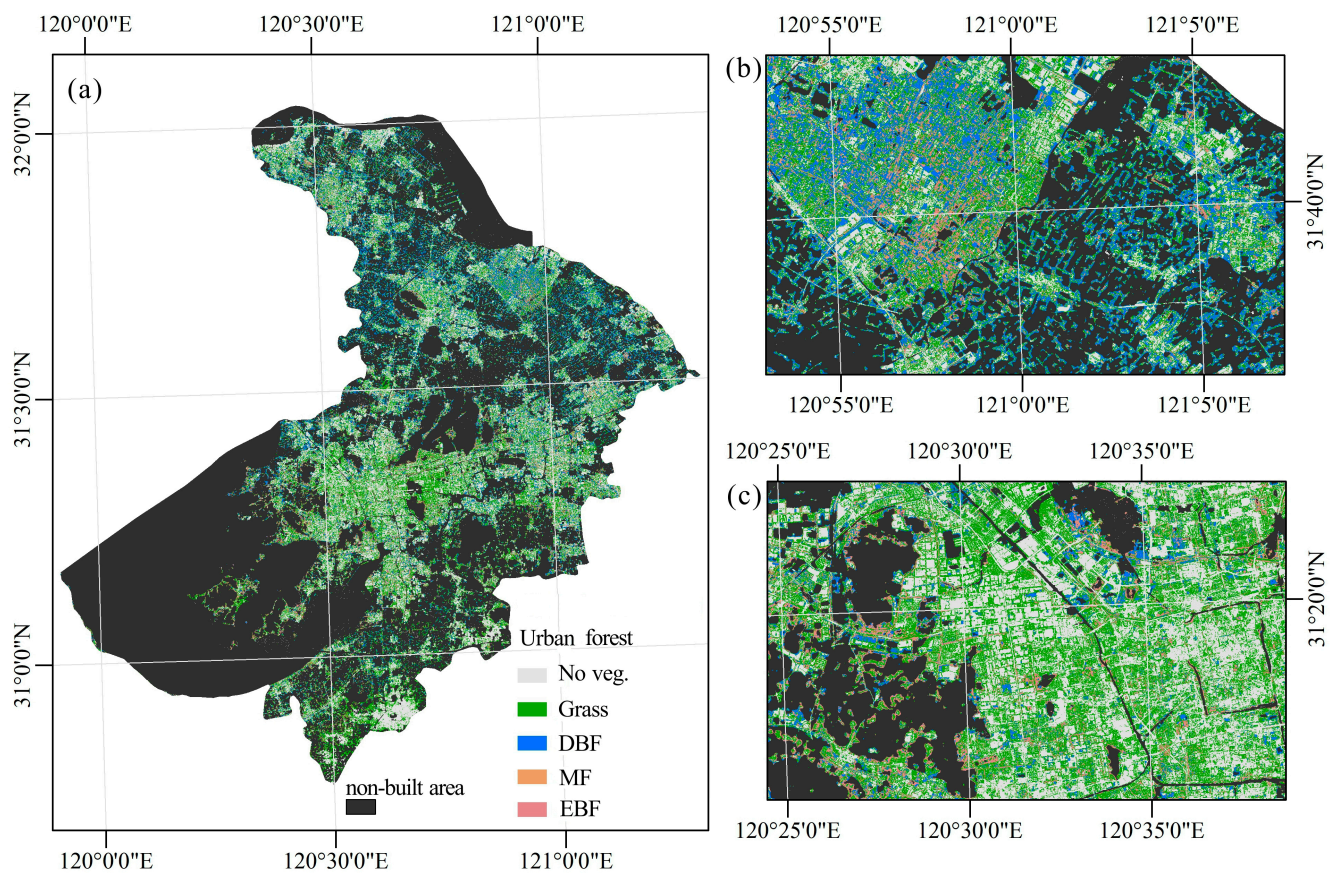
Figure 9. The distribution of urban forests in Suzhou (**a**) and its detailed views (**b**,**c**). Veg. is vegetation. DBF, MF, and EBF are deciduous broadleaf forests, mixed forests, and evergreen broadleaf forests.

4. Discussion

4.1. Uncertainty of Estimating GPP by NIRv

Although, as we know, few studies have examined vegetation productivity in Suzhou, studies in similar cities may provide useful information. From 2000 to 2014, the average rate of GPP in Shanghai, the city next to Suzhou, was between 800 and 1050 g C m^{-2} yr^{-1} based on the simulations by Vegetation Photosynthesis Model (VPM) [55]. This result is close to our 973.74, 979.51, and 1074.21 g C m^{-2} yr^{-1} for MODIS, Landsat-8, and Sentinel-2, respectively.

According to the MOD17A2 product, the previous study also indicated the GPP of crops along the Yangtze River in the northeast of Suzhou as around 1200–1400 g C m^{-2} yr^{-1} [56], which is lower than our Sentinel-2 GPP, 1250–2000 g C m^{-2} yr^{-1}, in the same region (Figure 4d). Limited by mixed pixel effects, the MOD17A2 product usually overestimates in lower value and underestimates in higher value [57,58]. The high resolution of Sentinel-2 eliminated the many effects of the mixed pixel. Therefore, the Sentinel-2 GPP was obviously higher than the GPP calculated by MODIS reflectance. Furthermore, Landsat-8 GPP would have to be greater than MODIS GPP if it did not miss images during July and August, when carbon assimilation rates are at their peak.

Compared to deciduous forests, evergreen forests are inflexible to short-term changes in environmental conditions. As a result, their NIRv is suitable for predicting GPP over a longer period, such as 90 days [25]. Consequently, the NIRv–GPP relationship is a challenge in estimating monthly GPP for evergreen forests. Additionally, for this reason, our GPP of evergreen forests in the southwest of Suzhou was more than 2500 g C m^{-2} yr^{-1}, which is higher than the previously observed and simulated results [59,60]. Additionally, the original NIRv-GPP relationships across the different land cover types are generated by 0.05 degree AVHRR reflectance [23]. The uncertainty induced by the different remote

sensing data in terms of field of view angle, signal-to-noise ratio, and spectral width needs to be further evaluated.

4.2. Evaluation of High-Resolution Remote Sensing Images in Urban Carbon Research

Compared to Landsat-8 and Sentinel-2, the lower resolution of MODIS lost many details inside the city (Figure 4b–d). In the built areas, vegetation usually accounts for a small proportion at 500 m resolution. As a result, the reflection characteristics of vegetation will be affected by the background. Meanwhile, due to the variety of land cover types within a built area, low-resolution remote sensing images fail to accurately depict the spatial variability of urban surfaces (Figure 10), thereby excluding changes in vegetation characteristics within the city. As a result, the uncertainty in estimating GPP from low remote sensing images increases. As Figure 11 shows, with the increment of spatial resolution, the contribution of the urban forest to total GPP was increased. Therefore, the photosynthetic ability of urban forests can be better figured out by fine-resolution remote sensing images. Landsat having similar performance as MODIS is partially due to its coarser resolution and lower NDVI relative to Sentinel-2, and also partially owing to missing data of high values in summer with large fractions of cloudy days.
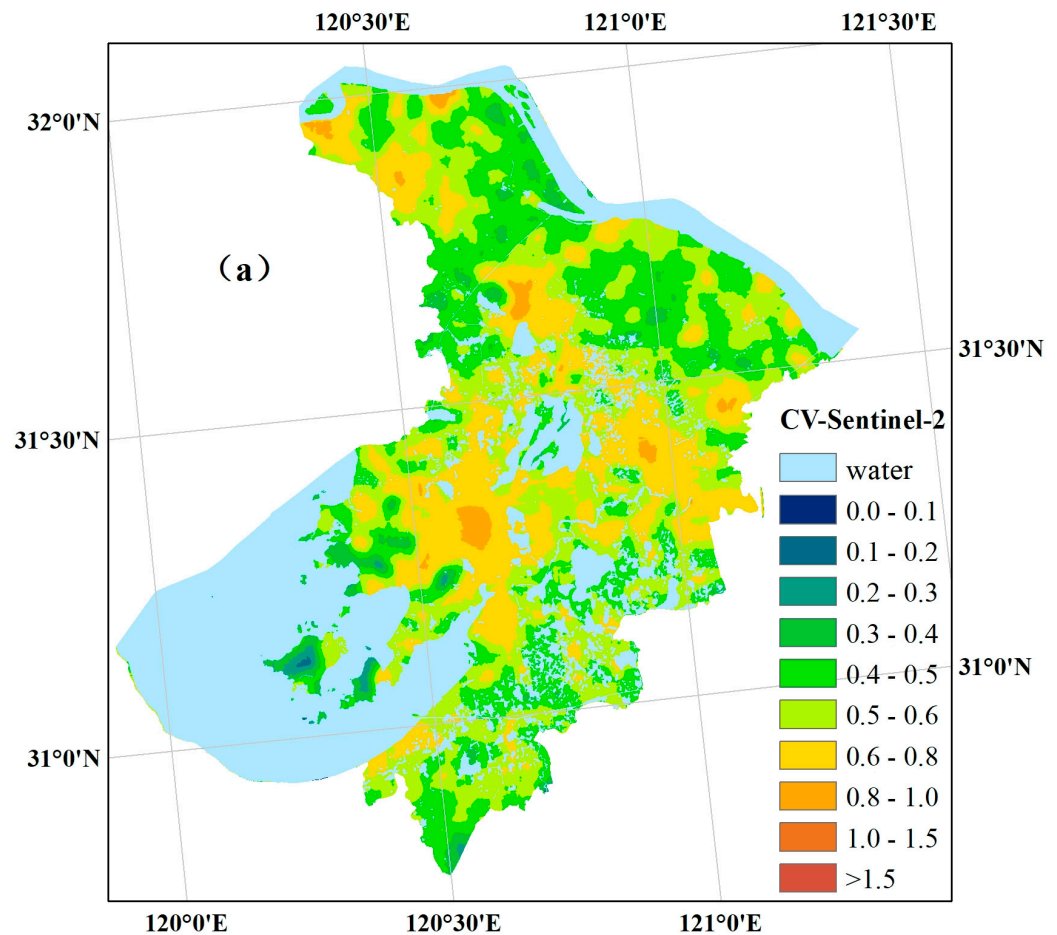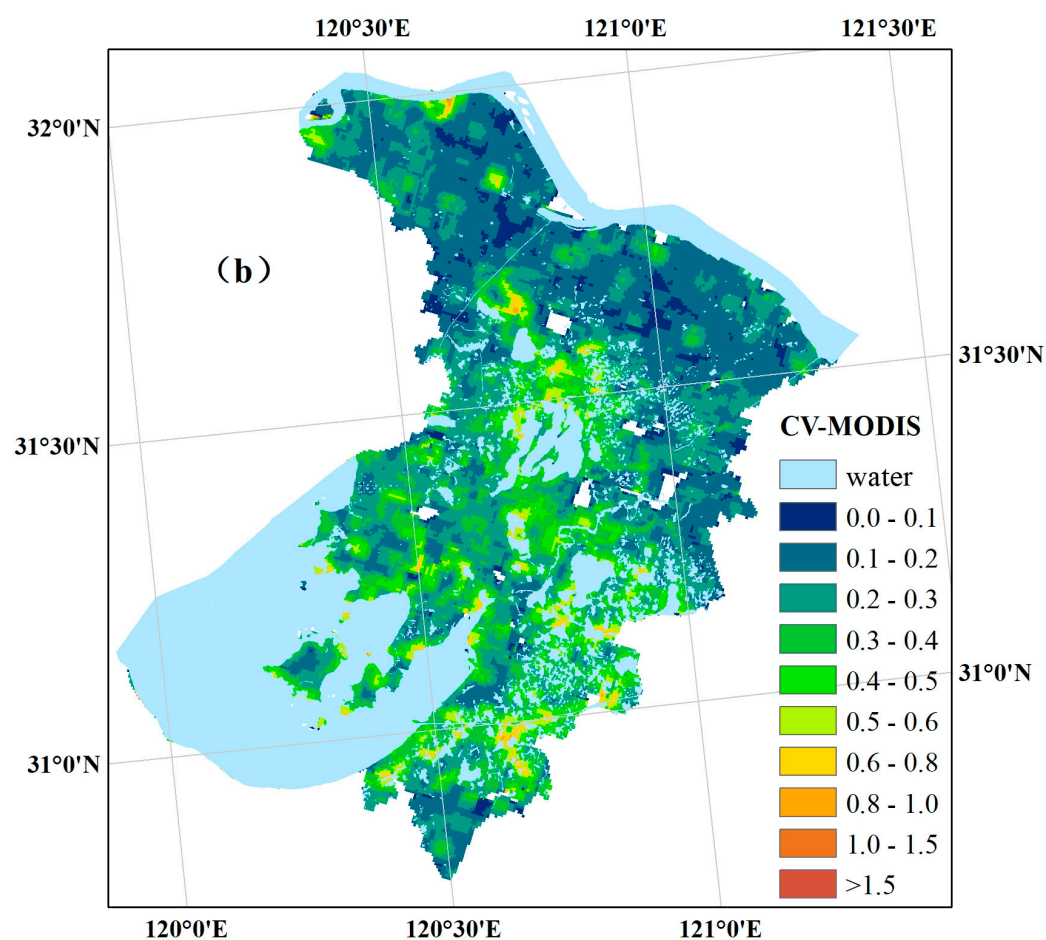

Figure 10. *Cont.*

Figure 10. The GPP variation coefficient (CV) of Sentinel-2 (**a**) and MODIS (**b**).
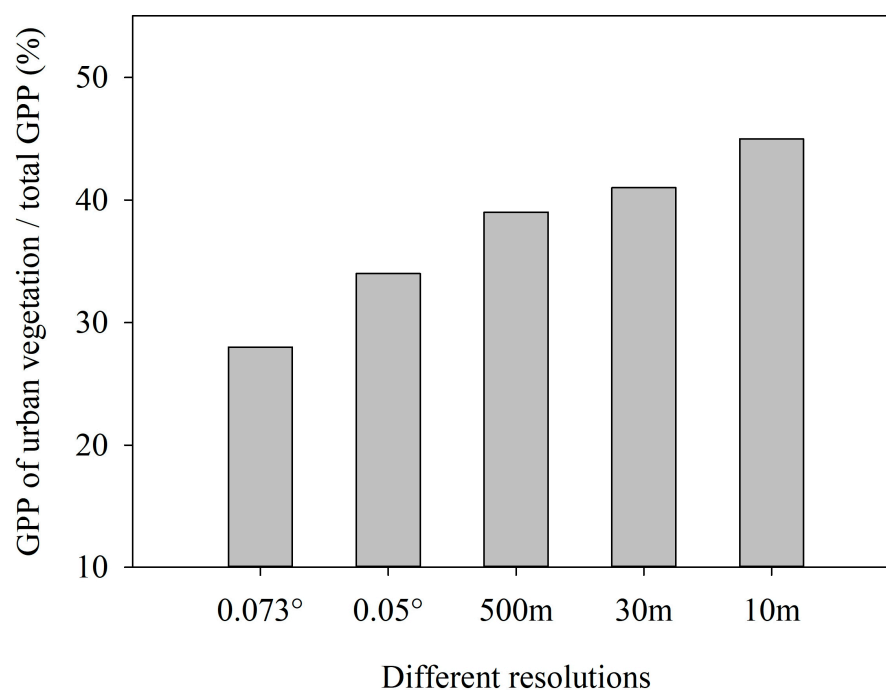

Figure 11. The contribution of urban forests to total GPP. The percentages of 0.073° and 0.05° are from Ju [51] and Zhang [50], respectively. Additionally, results of 500, 30, and 10 m resolutions were calculated by MODIS, Landsat-8 and Sentinel-2 in this study.

With its 10 m resolution, the Sentinel-2 GPP can provide more information about vegetation dynamics in built areas. Despite the fact that Landsat-8 GPP has a relatively high resolution to explore the dynamic of urban forests, the 16-day revisiting period made the images of Landsat-8 subject to cloud cover. For example, for July and August of 2021, the whole regional average NIRv of Landsat 8 cannot be generated. Vegetation is at a growing peak during these two months, which is vital for the yearly total GPP. Therefore, the 5-day revisiting period and higher spatial resolution of Sentinel-2 images make them ideal for studying GPP on an urban scale.

4.3. Importance of Urban Forests for Regional Carbon Budget

In the land process-based model, as well as the remote sensing model, urban built areas are usually masked according to land cover data based on the hypothesis that the photosynthesis of urban forest is weak [45,47]. However, our study illustrated that the photosynthetic capacity of urban forest was also considerable (Table 3). Meanwhile, in Suzhou, the coverage of urban forest was 2253.1 km^2, which was significantly higher than the 371.9 km^2 of vegetation in non-built area. As a result, about 44.43% of the total GPP in Suzhou was contributed by urban forests (Figure 3). Therefore, the GPP of urban forest is an important part of the regional carbon budget and should not be ignored.

Table 3. Differences in yearly GPP between vegetation in non-built areas and built area.

Veg. Type	Non-Built Area (g C m^{-2} yr^{-1})	Urban Forest (g C m^{-2} yr^{-1})
GRA	2275.9 ± 949.8	841.5 ± 599.2
DBF	2500.9 ± 749.0	1589.7 ± 722.0
MF	2306.1 ± 605.6	1478.4 ± 624.4
EBF	3206.6 ± 507.4	2640.6 ± 478.8

Note: GRA, DBF, MF, and EBF are grassland, deciduous broadleaf forest, mixed forest, and evergreen broadleaf forest, respectively. Urban forest is the GRA, DBF, MF, and EBF in the built area.

The average GPP of urban forests was significantly lower (about 36.3%) than the average GPP of vegetation in the non-built area (Table 3). This reduction of GPP can primarily be attributed to many factors related to human activities in built areas [61,62]. From an ecological perspective, urban forests are highly fragmented and, as a result, they are vulnerable to human activities [63]. Additionally, in view of the atmosphere environment, urban forests are usually exposed to a high concentration of PM2.5 and O$_3$, which damages leaf tissue and affects photosynthesis [64]. However, the urban environment also includes some positive factors for carbon assimilation, for example, the increment in temperature due to the heat island effect [61,65], high CO$_2$ concentration from greenhouse gas emission [45,66], and enhanced nitrogen deposition from fossil fuel [67]. If we can improve the management of urban forests to maximize positive factors that promote carbon assimilation, urban forests will be able to play a more significant role in regional carbon budgets, which will help China achieve the target of carbon neutrality.

5. Conclusions

In this study, MODIS, Landsat-8 and Sentinel-2 images were used to generate regional GPP in one of China's most economically developed cities, Suzhou, to identify the applicability of different kinds of remote sensing data on urban scale studies and the characteristics of urban carbon budgets. The results of GPP estimated by MODIS, Landsat-8, and Sentinel-2 images were 8.43, 8.48, and 9.30 Tg C yr^{-1}, respectively. The monthly dynamic of GPP exhibited two peaks in April and September. In May, the harvest of wheat and the pruning process conducted on urban forests made a pronounced decline in total GPP by about 25.93% according to Sentinel-2. Accordingly, climate factors as well as anthropogenic factors contribute to the change of urban GPP. As the spatial resolution rose, the contribution of the urban forest to regional total GPP increased, reaching about 44.63% according to the 10 m sentinel-2 images. Since the distribution of urban forests is highly fragmental,

high-resolution remote sensing images can better figure out the dynamic changes in the GPP of the urban forest. The results of our study demonstrate the importance of using high-resolution remote sensing images for estimating the GPP of the urban forest and for improving our understanding of the urban carbon budget.

References

1. Anav, A.; Friedlingstein, P.; Beer, C.; Ciais, P.; Harper, A.; Jones, C.; Murray-Tortarolo, G.; Papale, D.; Parazoo, N.C.; Peylin, P.; et al. Spatiotemporal patterns of terrestrial gross primary production: A review. *Rev. Geophys.* **2015**, *53*, 785–818. [CrossRef]
2. Zheng, Y.; Shen, R.; Wang, Y.; Li, X.; Liu, S.; Liang, S.; Chen, J.M.; Ju, W.; Zhang, L.; Yuan, W. Improved estimate of global gross primary production for reproducing its long-term variation, 1982–2017. *Earth Syst. Sci. Data* **2020**, *12*, 2725–2746. [CrossRef]
3. Jian, J.; Bailey, V.; Dorheim, K.; Konings, A.G.; Hao, D.; Shiklomanov, A.N.; Snyder, A.; Steele, M.; Teramoto, M.; Vargas, R.; et al. Historically inconsistent productivity and respiration fluxes in the global terrestrial carbon cycle. *Nat. Commun.* **2022**, *13*, 1733. [CrossRef] [PubMed]
4. Baldocchi, D.; Falge, E.; Gu, L.; Olson, R.; Hollinger, D.; Running, S.; Anthoni, P.; Bernhofer, C.; Davis, K.; Evans, R.; et al. FLUXNET: A new tool to study the temporal and spatial variability of ecosystem-scale carbon dioxide, water vapor, and energy flux densities. *Bull. Am. Meteorol. Soc.* **2001**, *82*, 2415–2434. [CrossRef]
5. Beer, C.; Reichstein, M.; Tomelleri, E.; Ciais, P.; Jung, M.; Carvalhais, N.; Rödenbeck, C.; Arain, M.A.; Baldocchi, D.; Bonan, G.B.; et al. Terrestrial gross carbon dioxide uptake: Global distribution and covariation with climate. *Science* **2010**, *329*, 834–838. [CrossRef] [PubMed]
6. Jung, M.; Reichstein, M.; Margolis, H.A.; Cescatti, A.; Richardson, A.D.; Arain, M.A.; Arneth, A.; Bernhofer, C.; Bonal, D.; Chen, J.; et al. Global patterns of land-atmosphere fluxes of carbon dioxide, latent heat, and sensible heat derived from eddy covariance, satellite, and meteorological observations. *J. Geophys. Res. Biogeosci.* **2011**, *116*, G00J07. [CrossRef]
7. Jiang, C.; Ryu, Y. Multi-scale evaluation of global gross primary productivity and evapotranspiration products derived from Breathing Earth System Simulator (BESS). *Remote Sens. Environ.* **2016**, *186*, 528–547. [CrossRef]
8. Qiu, B.; Chen, J.M.; Ju, W.; Zhang, Q.; Zhang, Y. Simulating emission and scattering of solar-induced chlorophyll fluorescence at far-red band in global vegetation with different canopy structures. *Remote Sens. Environ.* **2019**, *233*, 111373. [CrossRef]
9. Wu, Z.; Ahlström, A.; Smith, B.; Ardö, J.; Eklundh, L.; Fensholt, R.; Lehsten, V. Climate data induced uncertainty in model-based estimations of terrestrial primary productivity. *Environ. Res. Lett.* **2017**, *12*, 064013. [CrossRef]
10. Running, S.W.; Nemani, R.R.; Heinsch, F.A.; Zhao, M.; Reeves, M.; Hashimoto, H. A continuous satellite-derived measure of global terrestrial primary production. *BioScience* **2004**, *54*, 547–560. [CrossRef]
11. Zhang, Z.; Zhang, Y.; Zhang, Y.; Gobron, N.; Frankenberg, C.; Wang, S.; Li, Z. The potential of satellite FPAR product for GPP estimation: An indirect evaluation using solar-induced chlorophyll fluorescence. *Remote Sens. Environ.* **2020**, *240*, 111686. [CrossRef]
12. Damm, A.; Elbers, J.A.N.; Erler, A.; Gioli, B.; Hamdi, K.; Hutjes, R.; Kosvancova, M.; Meroni, M.; Miglietta, F.; Moersch, A.; et al. Remote sensing of sun-induced fluorescence to improve modeling of diurnal courses of gross primary production (GPP). *Glob. Chang. Biol.* **2010**, *16*, 171–186. [CrossRef]
13. Zhang, Y.; Guanter, L.; Berry, J.A.; van der Tol, C.; Yang, X.; Tang, J.; Zhang, F. Model-based analysis of the relationship between sun-induced chlorophyll fluorescence and gross primary production for remote sensing applications. *Remote Sens. Environ.* **2016**, *187*, 145–155. [CrossRef]

14. Wu, C.; Chen, J.M.; Huang, N. Predicting gross primary production from the enhanced vegetation index and photosynthetically active radiation: Evaluation and calibration. *Remote Sens. Environ.* **2011**, *115*, 3424–3435. [CrossRef]

15. Wu, C.; Niu, Z.; Gao, S. Gross primary production estimation from MODIS data with vegetation index and photosynthetically active radiation in maize. *J. Geophys. Res. Atmos.* **2010**, *115*, D12127. [CrossRef]

16. Guanter, L.; Zhang, Y.; Jung, M.; Joiner, J.; Voigt, M.; Berry, J.A.; Frankenberg, C.; Huete, A.R.; Zarco-Tejada, P.; Lee, J.E.; et al. Global and time-resolved monitoring of crop photosynthesis with chlorophyll fluorescence. *Proc. Natl. Acad. Sci. USA* **2014**, *111*, E1327–E1333. [CrossRef]

17. Zhang, J.; Xiao, J.; Tong, X.; Zhang, J.; Meng, P.; Li, J.; Liu, P.; Yu, P. NIRv and SIF better estimate phenology than NDVI and EVI: Effects of spring and autumn phenology on ecosystem production of planted forests. *Agric. For. Meteorol.* **2022**, *315*, 108819. [CrossRef]

18. Wang, R.; Gamon, J.A.; Emmerton, C.A.; Springer, K.R.; Yu, R.; Hmimina, G. Detecting intra-and inter-annual variability in gross primary productivity of a North American grassland using MODIS MAIAC data. *Agric. For. Meteorol.* **2020**, *281*, 107859. [CrossRef]

19. Shi, H.; Li, L.; Eamus, D.; Huete, A.; Cleverly, J.; Tian, X.; Yu, Q.; Wang, S.; Montagnani, L.; Magliulo, V.; et al. Assessing the ability of MODIS EVI to estimate terrestrial ecosystem gross primary production of multiple land cover types. *Ecol. Indic.* **2017**, *72*, 153–164. [CrossRef]

20. Li, X.; Xiao, J. TROPOMI observations allow for robust exploration of the relationship between solar-induced chlorophyll fluorescence and terrestrial gross primary production. *Remote Sens. Environ.* **2022**, *268*, 112748. [CrossRef]

21. Baldocchi, D.D.; Ryu, Y.; Dechant, B.; Eichelmann, E.; Hemes, K.; Ma, S.; Sanchez, C.R.; Shortt, R.; Szutu, D.; Valach, A.; et al. Outgoing near-infrared radiation from vegetation scales with canopy photosynthesis across a spectrum of function, structure, physiological capacity, and weather. *J. Geophys. Res. Biogeosci.* **2020**, *125*, e2019JG005534. [CrossRef]

22. Zhang, Y.; Joiner, J.; Gentine, P.; Zhou, S. Reduced solar-induced chlorophyll fluorescence from GOME-2 during Amazon drought caused by dataset artifacts. *Glob. Chang. Biol.* **2018**, *24*, 2229–2230. [CrossRef] [PubMed]

23. Wang, S.; Zhang, Y.; Ju, W.; Qiu, B.; Zhang, Z. Tracking the seasonal and inter-annual variations of global gross primary production during last four decades using satellite near-infrared reflectance data. *Sci. Total Environ.* **2021**, *755*, 142569. [CrossRef]

24. Badgley, G.; Field, C.B.; Berry, J.A. Canopy near-infrared reflectance and terrestrial photosynthesis. *Sci. Adv.* **2017**, *3*, e1602244. [CrossRef]

25. Badgley, G.; Anderegg, L.D.; Berry, J.A.; Field, C.B. Terrestrial gross primary production: Using NIRV to scale from site to globe. *Glob. Chang. Biol.* **2019**, *25*, 3731–3740. [CrossRef] [PubMed]

26. Wu, G.; Guan, K.; Jiang, C.; Peng, B.; Kimm, H.; Chen, M.; Yang, X.; Wang, S.; Suyker, A.E.; Bernacchi, C.J.; et al. Radiance-based NIRv as a proxy for GPP of corn and soybean. *Environ. Res. Lett.* **2020**, *15*, 034009. [CrossRef]

27. Mengistu, A.G.; Mengistu Tsidu, G.; Koren, G.; Kooreman, M.L.; Boersma, K.F.; Tagesson, T.; Ardö, J.; Nouvellon, Y.; Peters, W. Sun-induced fluorescence and near-infrared reflectance of vegetation track the seasonal dynamics of gross primary production over Africa. *Biogeosciences* **2021**, *18*, 2843–2857. [CrossRef]

28. Qiao, K.; Zhu, W.; Xie, Z.; Li, P. Estimating the seasonal dynamics of the leaf area index using piecewise LAI-VI relationships based on phenophases. *Remote Sens.* **2019**, *11*, 689. [CrossRef]

29. Camps-Valls, G.; Campos-Taberner, M.; Moreno-Martínez, Á.; Walther, S.; Duveiller, G.; Cescatti, A.; Mahecha, M.D.; Muñoz-Marí, J.; García-Haro, F.J.; Guanter, L.; et al. A unified vegetation index for quantifying the terrestrial biosphere. *Sci. Adv.* **2021**, *7*, eabc7447. [CrossRef]

30. Yang, R.; Wang, J.; Zeng, N.; Sitch, S.; Tang, W.; McGrath, M.J.; Cai, Q.; Liu, D.; Lombardozzi, D.; Tian, H.; et al. Divergent historical GPP trends among state-of-the-art multi-model simulations and satellite-based products. *Earth Syst. Dyn.* **2022**, *13*, 833–849. [CrossRef]

31. Merrick, T.; Pau, S.; Detto, M.; Broadbent, E.N.; Bohlman, S.A.; Still, C.J.; Almeyda Zambrano, A.M. Unveiling spatial and temporal heterogeneity of a tropical forest canopy using high-resolution NIRv, FCVI, and NIRvrad from UAS observations. *Biogeosciences* **2021**, *18*, 6077–6091. [CrossRef]

32. Dechant, B.; Ryu, Y.; Badgley, G.; Zeng, Y.; Berry, J.A.; Zhang, Y.; Goulas, Y.; Li, Z.; Zhang, Q.; Kang, M.; et al. Canopy structure explains the relationship between photosynthesis and sun-induced chlorophyll fluorescence in crops. *Remote Sens. Environ.* **2020**, *241*, 111733. [CrossRef]

33. Zeng, Y.; Badgley, G.; Dechant, B.; Ryu, Y.; Chen, M.; Berry, J.A. A practical approach for estimating the escape ratio of near-infrared solar-induced chlorophyll fluorescence. *Remote Sens. Environ.* **2019**, *232*, 111209. [CrossRef]

34. Escobedo, F.J.; Wagner, J.E.; Nowak, D.J.; De la Maza, C.L.; Rodriguez, M.; Crane, D.E. Analyzing the cost effectiveness of Santiago, Chile's policy of using urban forests to improve air quality. *J. Environ. Manag.* **2008**, *86*, 148–157. [CrossRef]

35. Escobedo, F.J.; Adams, D.C.; Timilsina, N. Urban forest structure effects on property value. *Ecosyst. Serv.* **2015**, *12*, 209–217. [CrossRef]

36. Lee, S.J.; Longcore, T.; Rich, C.; Wilson, J.P. Increased home size and hardscape decreases urban forest cover in Los Angeles County's single-family residential neighborhoods. *Urban For. Urban Green.* **2017**, *24*, 222–235. [CrossRef]

37. Ren, Z.; He, X.; Pu, R.; Zheng, H. The impact of urban forest structure and its spatial location on urban cool island intensity. *Urban Ecosyst.* **2018**, *21*, 863–874. [CrossRef]

38. Roeland, S.; Moretti, M.; Amorim, J.H.; Branquinho, C.; Fares, S.; Morelli, F.; Niinemets, Ü.; Paoletti, E.; Pinho, P.; Sgrigna, G.; et al. Towards an integrative approach to evaluate the environmental ecosystem services provided by urban forest. *J. For. Res.* **2019**, *30*, 1981–1996. [CrossRef]

39. Davies, Z.G.; Edmondson, J.L.; Heinemeyer, A.; Leake, J.R.; Gaston, K.J. Mapping an urban ecosystem service: Quantifying above-ground carbon storage at a city-wide scale. *J. Appl. Ecol.* **2011**, *48*, 1125–1134. [CrossRef]

40. Myeong, S.; Nowak, D.J.; Duggin, M.J. A temporal analysis of urban forest carbon storage using remote sensing. *Remote Sens. Environ.* **2006**, *101*, 277–282. [CrossRef]

41. Agbelade, A.D.; Onyekwelu, J.C. Tree species diversity, volume yield, biomass and carbon sequestration in urban forests in two Nigerian cities. *Urban Ecosyst.* **2020**, *23*, 957–970. [CrossRef]

42. Wang, S.; Ju, W.; Peñuelas, J.; Cescatti, A.; Zhou, Y.; Fu, Y.; Huete, A.; Liu, M.; Zhang, Y. Urban–rural gradients reveal joint control of elevated CO_2 and temperature on extended photosynthetic seasons. *Nat. Ecol. Evol.* **2019**, *3*, 1076–1085. [CrossRef] [PubMed]

43. Zhang, Y.; Meng, W.; Yun, H.; Xu, W.; Hu, B.; He, M.; Mo, X.; Zhang, L. Is urban green space a carbon sink or source?—A case study of China based on LCA method. *Environ. Impact Assess. Rev.* **2022**, *94*, 106766. [CrossRef]

44. Zhao, M.S.; Running, S.; Heinsch, F.A.; Nemani, R. MODIS-Derived Terrestrial Primary Production. In *Land Remote Sensing and Global Environmental Change*; Ramachandran, B., Justice, C.O., Abrams, M.J., Eds.; Springer: New York, NY, USA, 2010; pp. 635–660.

45. Zhao, T.; Brown, D.G.; Bergen, K.M. Increasing gross primary production (GPP) in the urbanizing landscapes of southeastern Michigan. *Photogramm. Eng. Remote Sens.* **2007**, *73*, 1159–1167. [CrossRef]

46. Ding, Z.; Zheng, H.; Li, H.; Yu, P.; Man, W.; Liu, M.; Tang, X.; Liu, Y. Afforestation-driven increases in terrestrial gross primary productivity are partly offset by urban expansion in Southwest China. *Ecol. Indic.* **2021**, *127*, 107641. [CrossRef]

47. Cui, Y.; Xiao, X.; Dong, J.; Zhang, Y.; Qin, Y.; Doughty, R.B.; Wu, X.; Liu, X.; Joiner, J.; Moore, B., III. Continued Increases of Gross Primary Production in Urban Areas during 2000–2016. *J. Remote Sens.* **2022**, *2022*, 9868564. [CrossRef]

48. Karra, K.; Kontgis, C.; Statman-Weil, Z.; Mazzariello, J.C.; Mathis, M.; Brumby, S.P. Global land use/land cover with Sentinel 2 and deep learning. In Proceedings of the 2021 IEEE International Geoscience and Remote Sensing Symposium IGARSS, Brussels, Belgium, 11–16 July 2021; pp. 4704–4707.

49. Li, X.B.; Shi, P. Sensitivity analysis of variation in NDVI, temperature and precipitation in typical vegetation types a across China. *Chin. J. Plant Ecol.* **2000**, *24*, 379.

50. Zhang, Y.; Xiao, X.; Wu, X.; Zhou, S.; Zhang, G.; Qin, Y.; Dong, J. A global moderate resolution dataset of gross primary production of vegetation for 2000–2016. *Sci. Data* **2015**, *4*, 170165. [CrossRef]

51. Ju, W.M.; Zhou, Y.L. *Global Daily GPP Simulated Data Products from 1981 to 2019 [DB/OL]*; National Ecosystem Science Data Center: Beijing, China, 2021. [CrossRef]

52. He, M.; Ju, W.; Zhou, Y.; Chen, J.; He, H.; Wang, S.; Wang, H.; Guan, D.; Yan, J.; Li, Y.; et al. Development of a two-leaf light use efficiency model for improving the calculation of terrestrial gross primary productivity. *Agric. For. Meteorol.* **2013**, *173*, 28–39. [CrossRef]

53. Zhou, H.; Xu, M.; Pan, H.; Yu, X. Leaf-age effects on temperature responses of photosynthesis and respiration of an alpine oak, Quercus aquifolioides, in southwestern China. *Tree Physiol.* **2015**, *35*, 1236–1248. [CrossRef]

54. Haberl, H.; Erb, K.H.; Krausmann, F.; Gaube, V.; Bondeau, A.; Plutzar, C.; Gingrich, S.; Lucht, W.; Fischer-Kowalski, M. Quantifying and mapping the human appropriation of net primary production in earth's terrestrial ecosystems. *Proc. Natl. Acad. Sci. USA* **2007**, *104*, 12942–12947. [CrossRef] [PubMed]

55. Cui, Y.; Xiao, X.; Zhang, Y.; Dong, J.; Qin, Y.; Doughty, R.B.; Zhang, G.; Wang, J.; Wu, X.; Qin, Y.; et al. Temporal consistency between gross primary production and solar-induced chlorophyll fluorescence in the ten most populous megacity areas over years. *Sci. Rep.* **2017**, *7*, 14963. [CrossRef] [PubMed]

56. Wang, F.; Jiang, H.; Zhang, X. Spatial–temporal dynamics of gross primary productivity, evapotranspiration, and water-use efficiency in the terrestrial ecosystems of the Yangtze River Delta region and their relations to climatic variables. *Int. J. Remote Sens.* **2015**, *36*, 2654–2673. [CrossRef]

57. Wang, L.; Zhu, H.; Lin, A.; Zou, L.; Qin, W.; Du, Q. Evaluation of the latest MODIS GPP products across multiple biomes using global eddy covariance flux data. *Remote Sens.* **2017**, *9*, 418. [CrossRef]

58. Zhang, F.; Chen, J.M.; Chen, J.; Gough, C.M.; Martin, T.A.; Dragoni, D. Evaluating spatial and temporal patterns of MODIS GPP over the conterminous US against flux measurements and a process model. *Remote Sens. Environ.* **2012**, *124*, 717–729. [CrossRef]

59. Chen, Y.; Gu, H.; Wang, M.; Gu, Q.; Ding, Z.; Ma, M.; Liu, R.; Tang, X. Contrasting performance of the remotely-derived GPP products over different climate zones across China. *Remote Sens.* **2019**, *11*, 1855. [CrossRef]

60. Liu, Z.; Wang, L.; Wang, S. Comparison of different GPP models in China using MODIS image and ChinaFLUX data. *Remote Sens.* **2014**, *6*, 10215–10231. [CrossRef]

61. Zhang, L.; Yang, L.; Zohner, C.M.; Crowther, T.W.; Li, M.; Shen, F.; Guo, M.; Qin, J.; Yao, L.; Zhou, C. Direct and indirect impacts of urbanization on vegetation growth across the world's cities. *Sci. Adv.* **2022**, *8*, eabo0095. [CrossRef]

62. Nuarsa, I.W.; As-syakur, A.R.; Gunadi, I.G.A.; Sukewijaya, I.M. Changes in Gross Primary Production (GPP) over the past two decades due to land use conversion in a tourism city. *ISPRS Int. J. Geo-Inf.* **2018**, *7*, 57. [CrossRef]

63. Ren, Y.; Yan, J.; Wei, X.; Wang, Y.; Yang, Y.; Hua, L.; Xiong, Y.; Niu, X.; Song, X.J. Effects of rapid urban sprawl on urban forest carbon stocks: Integrating remotely sensed, GIS and forest inventory data. *J. Environ. Manag.* **2012**, *113*, 447–455. [CrossRef]

64. Li, Y.; Wang, Y.; Wang, B.; Wang, Y.; Yu, W. The response of plant photosynthesis and stomatal conductance to fine particulate matter (PM2. 5) based on leaf factors analyzing. *J. Plant Biol.* **2019**, *62*, 120–128. [CrossRef]

65. Peng, S.; Piao, S.; Ciais, P.; Friedlingstein, P.; Ottle, C.; Bréon, F.M.; Nan, H.; Zhou, L.; Myneni, R.B. Surface urban heat island across 419 global big cities. *Environ. Sci. Technol.* **2012**, *46*, 696–703. [CrossRef] [PubMed]

66. Marcotullio, P.J.; Sarzynski, A.; Albrecht, J.; Schulz, N.; Garcia, J. The geography of global urban greenhouse gas emissions: An exploratory analysis. *Clim. Chang.* **2013**, *121*, 621–634. [CrossRef]

67. Townsend, A.R.; Braswell, B.H.; Holland, E.A.; Penner, J.E. Spatial and temporal patterns in terrestrial carbon storage due to deposition of fossil fuel nitrogen. *Ecol. Appl.* **1996**, *6*, 806–814. [CrossRef]